The Astrophysical Journal, 826:146 (15pp), 2016 August 1 doi:10.3847/0004-637X/826/2/146

THE ENTIRE VIRIAL RADIUS OF THE FOSSIL CLUSTER RXJ 1159 + 5531. II. DARK MATTER AND BARYON FRACTION

David A. Buote[1], Yuanyuan Su[1,2], Fabio Gastaldello[3], and Fabrizio Brighenti[4]
[1] Department of Physics and Astronomy, University of California at Irvine, 4129 Frederick Reines Hall, Irvine, CA 92697-4575, USA
[2] Harvard-Smithsonian Center for Astrophysics, 60 Garden Street, Cambridge, MA 02138, USA
[3] INAF-IASF-Milano, Via E. Bassini 15, I-20133 Milano, Italy
[4] Dipartimento di Fisica e Astronomia, Universita di Bologna, via Ranzani 1, 40126 Bologa, Italy
Received 2016 February 29; revised 2016 April 27; accepted 2016 May 9; published 2016 July 27

ABSTRACT

In this second paper on the entire virial region of the relaxed fossil cluster RXJ 1159+5531, we present a hydrostatic analysis of the azimuthally averaged hot intracluster medium (ICM) using the results of Su et al. For a model consisting of ICM, stellar mass from the central galaxy (BCG), and an NFW dark matter (DM) halo, we obtain a good description of the projected radial profiles of ICM emissivity and temperature that yield precise constraints on the total mass profile. The BCG stellar mass component is clearly detected with a K-band stellar mass-to-light ratio, $M_\star/L_K = 0.61 \pm 0.11\ M_\odot/L_\odot$, consistent with stellar population synthesis models for a Milky Way initial mass function. We obtain a halo concentration, $c_{200} = 8.4 \pm 1.0$, and virial mass, $M_{200} = (7.9 \pm 0.6) \times 10^{13}\ M_\odot$. For its mass, the inferred concentration is larger than most relaxed halos produced in cosmological simulations with Planck parameters, consistent with RXJ 1159+5531 forming earlier than the general halo population. The baryon fraction at r_{200}, $f_{\rm b,200} = 0.134 \pm 0.007$, is slightly below the Planck value (0.155) for the universe. However, when we take into account the additional stellar baryons associated with non-central galaxies and the uncertain intracluster light (ICL), $f_{\rm b,200}$ increases by $\approx$0.015, consistent with the cosmic value and therefore no significant baryon loss from the system. The total mass profile is nearly a power law over a large radial range ($\sim$0.2–10 R_e), where the corresponding density slope α obeys the $\alpha - R_e$ scaling relation for massive early-type galaxies. Performing our analysis in the context of MOND still requires a large DM fraction (85.0% $\pm$ 2.5% at $r = 100$ kpc) similar to that obtained using the standard Newtonian approach. The detection of a plausible stellar BCG mass component distinct from the NFW DM halo in the total gravitational potential suggests that $\sim 10^{14}\ M_\odot$ represents the mass scale above which dissipation is unimportant in the formation of the central regions of galaxy clusters.

Key words: dark matter – galaxies: clusters: individual (RXJ 1159+5531) – galaxies: clusters: intracluster medium – X-rays: galaxies: clusters

1. INTRODUCTION

It is well appreciated that galaxy clusters are powerful tools for cosmological studies, especially through their halo mass function and global baryon fractions (e.g., Allen et al. 2011; Kravtsov & Borgani 2012). In order to obtain mass measurements of ever larger numbers of cluster masses at higher redshifts, studies must resort to global scaling relations, often involving proxies for the mass. Global scaling relations of intracluster medium (ICM) properties are particularly useful to probe cooling and feedback in cluster evolution. Measurements of global scaling relations must be interpreted within the context of a general paradigm (e.g., ΛCDM) that makes definite assumptions about the full radial structure of a halo. It is essential that those assumptions be verified for as many systems as possible through detailed radial mapping of halo properties.

Fortunately, there are several powerful probes of cluster mass distributions (e.g., galaxy kinematics, ICM temperature and density profiles, gravitational lensing, and SZ effect), which, ideally, can be combined to achieve the most accurate picture of cluster structure (e.g., Reiprich et al. 2013). In practice, different techniques are better suited for particular clusters because of multiple factors, such as distance and mass.

Well-known advantages of studying the ICM include (1) that it traces the three-dimensional cluster potential well; (2) the electron mean free path is sufficiently short (especially when considering the presence of weak magnetic fields) to guarantee that the fluid approximation holds (i.e., with an isotropic pressure tensor); and (3) the hydrostatic equilibrium approximation should apply within the virialized region, allowing the gravitating mass to be derived directly from the temperature and density profiles of the ICM (e.g., Sarazin 1986; Ettori et al. 2013).

Since clusters are still forming in the present epoch, deviations from the hydrostatic approximation are expected. Cosmological simulations expect typically 10%–30% of the total ICM pressure is non-thermal, primarily arising from random turbulent motions (e.g., Rasia et al. 2004; Nagai et al. 2007; Eckert et al. 2015). Even with the very unfortunate demise of *Astro-H*, eventually microcalorimeter detectors will provide for the first time precise direct measurements of ICM kinematics for many bright clusters, greatly reducing (or eliminating) this greatest source of systematic error in ICM studies (e.g., Kitayama et al. 2014). Even so, for the most reliable hydrostatic analysis it is desirable that the correction for non-thermal pressure be as small as possible; i.e., for the most relaxed systems.

It turns out to be difficult to find clusters with undisturbed ICM within their entire virial region. The clusters that tend to be the most dynamically relaxed over most of their virial region are the cool core clusters, which, unfortunately, are also those that most often display ICM disturbances in their central

regions believed to arise from intermittent feedback from an AGN in the central galaxy (e.g., Bykov et al. 2015). Hence, CC clusters with the least evidence for central ICM disturbance are probably the best clusters for hydrostatic studies.

The cool core fossil cluster RXJ 1159+5531 is especially well-suited for hydrostatic studies of its ICM. It is both sufficiently bright and distant ($z = 0.081$), allowing for its entire virial region to be mapped through a combination of *Chandra* and *Suzaku* observations with feasible total exposure time. The high-quality *Chandra* image reveals a highly regular ICM with no evidence of large, asymmetrical disturbances anywhere, including the central regions (Humphrey et al. 2012a). We have *Suzaku* observations covering the entire region within r_{200} on the sky and presented results for the ICM properties in each of four directions (including using the central *Chandra* observation) in Su et al. (2015, hereafter Paper 1). We found the ICM properties (e.g., temperature, density) to display only very modest azimuthal variations (<10%), providing evidence for a highly relaxed ICM.

In this second paper on the entire virial radius of RXJ 1159+5531, we focus on measurements of the BCG stellar mass-to-light ratio, dark matter (DM), gas, and baryon fraction. Whereas Paper 1 focused on the comparison of ICM properties obtained for each of the four directions observed by *Suzaku,* here we analyze results for all the directions together to obtain the best-fitting azimuthally averaged ICM and mass properties. For calculating distances we assumed a flat ΛCDM cosmology with $\Omega_{m,0} = 0.3$ and $H_0 = 70$ km s^{-1} Mpc^{-1}. At the redshift of RXJ 1159+5531 ($z = 0.081$) this translates to an angular-diameter distance of 315 Mpc and $1'' = 1.5$ kpc. Unless stated otherwise, all statistical uncertainties quoted in this paper are 1σ.

The paper is organized as follows. We review very briefly the observations, data preparation, and ICM measurements in Section 2. We discuss our implementation of the hydrostatic method in Section 3 and define the particular models and parameters in Section 4. We present the results in Section 5 and describe the construction of the systematic error budget in Section 6. Finally, in Section 7 we discuss several implications of our results and present our summary and conclusions in Section 8.

2. OBSERVATIONS

The observations and data preparation are reported in Paper 1, and we refer the interested reader to that paper for details. Briefly, after obtaining cleaned events files for each observation, we extracted spectra in several concentric circular annuli for each data set and constructed appropriate response files for each annulus; i.e., redistribution matrix files (RMFs) and auxiliary response files (ARFs, including "mixing" ARFs to account for the large, energy-dependent point-spread function of the *Suzaku* data). We constructed model *Suzaku* spectra representing the "non-cosmic" X-ray background (NXB) and subtracted these from the observations. All other background components for both the *Chandra* and *Suzaku* data were accounted for with simple parameterized models fitted directly to the observations using xspec v12.7.2 (Arnaud 1996); i.e., the annular spectrum of each data set was fitted individually with a complex spectral model consisting of components for the ICM and background. For each annulus on the sky, a single thermal plasma component (vapec) was fitted to represent all the ICM emission in that annulus. No deprojection was performed during the spectral fitting because it amplifies noise and renders the analysis of the background-dominated cluster outskirts even more challenging. Furthermore, standard deprojection algorithms (e.g., onion-peeling and projct in xspec) do not generally account for ICM emission outside the bounding annulus, which also can lead to sizable systematic effects (e.g., Nulsen & Bohringer 1995; McLaughlin 1999; Buote 2000a).

Consequently, the principal data products resulting from our analysis are the radial profiles of projected (1) emission-weighted temperature and (2) emissivity-weighted $\rho^2_{\rm gas}$; e.g., Equations (B10) and (B13) of Gastaldello et al. (2007). In addition, we also use the profile of projected, emission-weighted iron abundance ($Z_{\rm Fe}$) expressed in solar units (Asplund et al. 2006) to further constrain the emissivity in our hydrostatic models.

3. ENTROPY-BASED METHOD

We prefer to construct hydrostatic equilibrium models using an approach that begins by specifying a parameterized model for the ICM entropy (Humphrey et al. 2008). The benefits of this "entropy-based" approach, as well as a review of other methods, are presented in Buote & Humphrey (2012a). Compared to the temperature and density, the entropy profile is more slowly varying and has a well-motivated asymptotic form, $\sim r^{1.1}$ for all clusters (e.g., Tozzi & Norman 2001; Voit et al. 2005). In addition, by requiring the entropy to be a monotonically increasing function of radius, the additional contraint of convective stability (not typically applied in cluster mass studies) is easily enforced. We assume spherical symmetry, which, if in fact the cluster is a triaxial ellipsoid, introduces only modest biases into the inferred parameters (see Section 6.1).

For studies of cluster ICM the thermodynamic entropy is usually replaced by the entropy proxy, $S \equiv k_{\rm B} T n_e^{-2/3}$, expressed in units of keV cm^2. It is useful to define the quantity, $S_\rho \equiv (k_{\rm B}/\mu m_{\rm a}) T \rho_{\rm gas}^{-2/3}$, where μ is the mean atomic mass of the ICM and m_a is the atomic mass unit, that replaces n_e in the entropy proxy with $\rho_{\rm gas}$ (e.g., using Equation (B4) of Gastaldello et al. 2007) so that

$$\frac{S_\rho}{S} = \frac{1}{\mu m_{\rm a}} \left(\frac{2+\mu}{5\mu} \frac{1}{m_{\rm a}} \right)^{2/3}. \quad (1)$$

The equation of hydrostatic equilibrium may now be written,

$$\frac{d\xi}{dr} = -\frac{2}{5} \frac{GM(<r)}{r^2} S_\rho^{-3/5} \quad (2)$$

where $\xi \equiv P^{2/5}$, P is the total thermal pressure, and $M(<r)$ is the total gravitating mass enclosed within radius r. Given S_ρ (after specifying S) and $M(<r)$, the hydrostatic equation can be integrated directly to obtain ξ and therefore the profiles of gas density, $\rho_{\rm gas} = (P/S_\rho)^{3/5} = S_\rho^{-3/5} \xi^{3/2}$, and temperature, $k_{\rm B} T/\mu m_{\rm a} = S_\rho^{3/5} P^{2/5} = S_\rho^{3/5} \xi$. By comparing the density and temperature profiles to the observations, we constrain the parameters of the input S and $M(<r)$ models.

Since $M(<r)$ in Equation (2) contains $M_{\rm gas}$, direct integration only yields a self-consistent solution for $\rho_{\rm gas}$ provided

$M_{\rm gas} \ll M(<r)$. In Paper 1, and all our previous studies of the entropy-based method, we ensured self-consistency in the case where $M_{\rm gas}$ cannot be neglected by differentiating the equation with respect to r and making use of the equation of mass continuity; e.g., see Equation (4) of Paper 1. Here we instead employ an iterative solution of Equation (2) by treating $M_{\rm gas}$ as a small perturbation. We solve Equation (2) initially by setting $M_{\rm gas} = 0$. From this solution we use the new $\rho_{\rm gas}$ to compute the profile of $M_{\rm gas}$. We then insert it into the hydrostatic equation and obtain an improved solution. The process is repeated until the value of $M_{\rm gas}$ near the virial radius changes by less than a desired amount.

A boundary condition on ξ must be specified to obtain a unique solution of Equation (2). We choose to specify the "reference pressure," $P_{\rm ref}$, at a radius of 10 kpc. Hence, the free parameters in our hydrostatic model are $P_{\rm ref}$ and those associated with S and $M(<r)$, which we detail below in Section 4.

To compare to the observations, the three-dimensional density and temperature profiles of the ICM obtained from Equation (2) are used to construct the volume emissivity, $\epsilon_\nu \propto \rho_{\rm gas}^2 \Lambda_\nu(T, Z)$, where $\Lambda_\nu(T, Z)$ is the ICM plasma emissivity. Then ϵ_ν and the emission-weighted temperature are projected onto the sky and averaged over the various circular annuli corresponding to the X-ray data using Equations (B10) and (B13) of Gastaldello et al. (2007). Since $\Lambda_\nu(T, Z)$ also depends on the metal abundances, we need to specify the abundance profiles in our models. As in our previous studies, we obtain best results by simply using the measured abundance profiles in projection and assigning them to be the true three-dimensional profiles for the models. (The iron abundance profiles are presented in Figure 3 of Humphrey et al. 2012a and Figure 13 of Paper 1.) In Section 6.8 we discuss instead using a parameterized model for the iron abundance that is emission weighted and projected onto the sky and fitted to the observations.

Since the X-ray emission in each annulus on the sky generally contains the sum of a range of temperatures and metallicities owing to radial gradients in the ICM properties, the values in particular of the temperature and metallicity obtained by fitting single-component ICM models to the projected spectra can be substantially biased with respect to the emission-weighted values (e.g., Buote 2000b; Mazzotta et al. 2004). To partially mitigate such biases in the data-model comparison, we employ "response weighting" of our projected models (see Equation (B15) of Gastaldello et al. 2007).

4. MODELS AND PARAMETERS

4.1. Entropy

For the ICM entropy profile we employ a power law with two breaks plus a constant,

$$S(r) = s_0 + s_1 f(r), \tag{3}$$

where s_0 represents a constant entropy floor, and $s_1 = S(r_{\rm ref}) - s_0$ for some reference radius $r_{\rm ref}$ (taken to be 10 kpc). The dimensionless function $f(r)$ is

$$f(r) = \begin{cases} \left(\dfrac{r}{r_{\rm ref}}\right)^{\alpha_1} & r \leqslant r_{\rm b,1} \\ f_1 \left(\dfrac{r}{r_{\rm ref}}\right)^{\alpha_2} & r_{\rm b,1} < r \leqslant r_{\rm b,2} \\ f_2 \left(\dfrac{r}{r_{\rm ref}}\right)^{\alpha_3} & r > r_{\rm b,2} \end{cases}$$

where $r_{\rm b,1}$ and $r_{\rm b,2}$ are the two break radii, and the coefficients f_1 and f_2 are given by

$$f_n = f_{n-1} \left(\frac{r_{{\rm b},n}}{r_{\rm ref}}\right)^{\alpha_n - \alpha_{n+1}},$$

with $f_0 \equiv 1$. To enforce convective stability (Section 3) we require $\alpha_1, \alpha_2, \alpha_3 \geqslant 0$. Hence, this model has seven free parameters: s_0, s_1, $r_{\rm b,1}$, $r_{\rm b,2}$, α_1, α_2, and α_3.

4.2. Stellar Mass

We represent the stellar mass of the cluster using the K-band light profile of the BCG (2MASX J11595215+5532053) from the Two Micron All-Sky Survey (2MASS) as listed in the Extended Source Catalog (Jarrett et al. 2000); i.e., an $n = 4$ Sérsic model (i.e., de Vaucouleurs) with $r_e = 9.83$ kpc and $L_K = 1.03 \times 10^{12}\, L_\odot$. Additional (poorly constrained) stellar mass contributions from non-central galaxies and intracluster light (ICL) are treated as a systematic error in Section 6.2.

4.3. Dark Matter

We consider the following models for the distribution of DM.

1. *NFW*. As it is the current standard both for modeling observations and simulated clusters, we use the NFW profile (Navarro et al. 1997) for our fiducial DM model. It has two free parameters, a concentration c_Δ, and mass M_Δ, evaluated with respect to an overdensity Δ times the critical density of the universe.
2. *Einasto*. The Einasto profile (Einasto 1965) is now recognized as a more accurate representation of the profiles of DM halos. We implement the mass profile following Merritt et al. (2006) but using the approximation for d_n given by Retana-Montenegro et al. (2012). As with the NFW profile, we express the parameters of the Einasto model in terms of a virial concentration, c_Δ, and mass, M_Δ. We fix $n = 5$ ($\alpha = 0.2$) appropriate for cluster halos (e.g., Dutton & Macciò 2014).
3. *CORELOG*. To provide a strong contrast to the NFW and Einasto models, we investigate a model having a constant density core and with a density that approaches r^{-2} at large radius. For consistency, we also express the free parameters of this model in terms of a virial concentration, c_Δ, and mass, M_Δ; e.g., see Section 2.1.2 of Buote & Humphrey (2012b) for more details.

All c_Δ, M_Δ, and r_Δ values are evaluated at the redshift of RXJ 1159+5531 (i.e., $z = 0.081$). Below we quote concentration values for the total mass profile (i.e., stars+gas+DM) as, $c_\Delta^{\rm tot} \equiv r_\Delta^{\rm tot}/r_s^{\rm DM}$, where $r_s^{\rm DM}$ is the DM scale radius and $r_\Delta^{\rm tot}$ is the

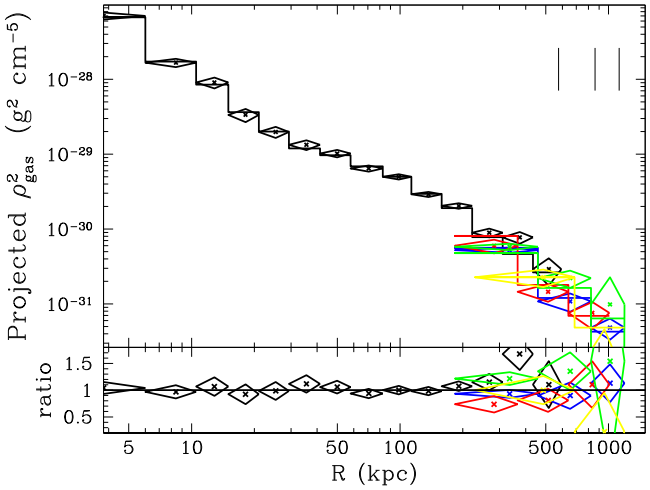

Figure 1. Quantity plotted (with 1σ errors) is proportional to the ICM surface brightness divided by $\Lambda_\nu(T, Z)$ (see Equation (B10) of Gastaldello et al. 2007). The best-fitting fiducial hydrostatic model is also overplotted so that its color reflects its value for each data set. The data sets are labeled as follows: *Chandra* (black); *Suzaku* pointings: N (blue), S (red), W (green), and E (yellow). The vertical lines in the top right corner indicate the best-fitting virial radii for the fiducial model; i.e., from left to right: r_{500}, r_{200}, and r_{108}. The bottom panel plots the data/model ratio.

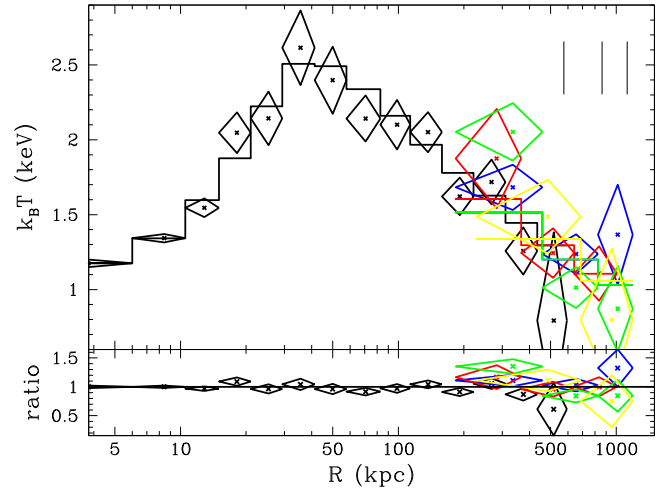

Figure 2. Projected emission-weighted hot gas temperature (k_{BT}) along with the best-fitting fiducial hydrostatic model in each circular annulus vs. radius R on the sky. The labeling scheme is the same as Figure 1.

virial radius of the total mass profile. We determine r_Δ^{tot} iteratively starting with the DM virial radius, adding in the baryon components, recomputing the virial radius, and stopping when the change in virial radius is less than a desired tolerance.

5. RESULTS

5.1. Overview

We fitted the model to the data using the "nested sampling" Bayesian Monte Carlo procedure implemented in the MultiNest code v2.18 (Feroz et al. 2009), and we adopted flat priors on the logarithms of all the free parameters. We used a χ^2 likelihood function, where the χ^2 consists of the temperature and projected ρ^2_{gas} data points, the model values, and the statistical weights. The weights are the variances of the data points obtained from the spectral fitting in Paper 1. We quote two "best" values for each parameter: (1) "Best Fit," which is the expectation value of the parameter in the derived posterior probability distribution, and (2) "Max Like," which is the parameter value that gives the maximum likelihood (found during the nested sampling). Finally, unless stated otherwise, all errors quoted are 1σ, representing the standard deviation of the parameter computed in the posterior probability distribution. All models shown in the figures have been evaluated using the "Max Like" values.

In Figures 1 and 2 we display the projected ρ^2_{gas} ($\propto \Sigma_\nu/\Lambda_\nu(T, Z)$, where Σ_ν is the surface brightness) and temperature data along with the best-fitting "fiducial" model (and residuals). The fiducial model consists of an entropy profile with two breaks, the $n = 4$ sersic model for the stellar mass of the BCG, and the NFW model for the DM. Inspection of the figures reveals that, overall, the fit is good. Most of the fit residuals are within $\approx 1\sigma$ of the model values, and the most deviant points lie within $\approx 2\sigma$ of the model values. Since for our Bayesian analysis we cannot easily formally assess the goodness-of-fit as in a frequentist approach, we have also fitted models to the data using a standard frequentist χ^2 analysis. For our fiducial model we obtain a minimum $\chi^2 = 39.9$ for 39 degrees of freedom, which is formally acceptable from the frequentist perspective. (For reference, if the BCG component is omitted, $\chi^2 = 59.6$; i.e., the data strongly require it.)

Below we shall often refer to the "Best Fit" virial radii of the fiducial model: $r_{2500} = 271$ kpc, $r_{500} = 575$ kpc, $r_{200} = 862$ kpc, and $r_{vir} = r_{108} = 1.12$ Mpc.

5.2. Entropy

The results for the entropy profile using the fiducial hydrostatic model are displayed in Figure 3, and the parameter constraints are listed in Table 1. In the figure we have plotted the "scaled" entropy in units of the characteristic entropy, $S_{500} = 260.6$ keV cm^2 (see Equation (3) of Pratt et al. 2010). The entropy profile has a small, but significant floor at the center and then rises more steeply than the $\sim r^{1.1}$ profile out to the first break radius ($\approx$36 kpc). The profile is then shallower than the baseline model out to the second break ($\approx$700 kpc), after which the slope is uncertain, but consistent with the baseline model out to the largest radii investigated ($\sim r_{108}$). As noted in Paper 1, at no radius does the scaled entropy fall below the baseline model, consistent with a simple feedback explanation. (See Paper 1 for more detailed discussion of how the entropy profile compares to theoretical models.)

In Figure 3 following Pratt et al. (2010) we also show the result of rescaling the entropy profile by $(f_{gas}/f_{b,U})^{2/3}$, where f_{gas} is the gas fraction as a function of radius and $f_{b,U} = 0.155$ is the baryon fraction of the universe. The overall very good agreement of this rescaled entropy profile with the baseline model suggests that the feedback has primarily served to spatially redistribute the gas rather than raise its temperature.

We note that the second break in the entropy profile is not required at high significance; i.e., the ratio of the Bayesian evidence for the two-break and one-break model is 1.9.

5.3. Pressure

The results for the pressure profile using the fiducial hydrostatic model are displayed in Figure 3, and the constraints for the reference pressure are listed in Table 1. In the figure we have plotted the "scaled" pressure in units of the characteristic

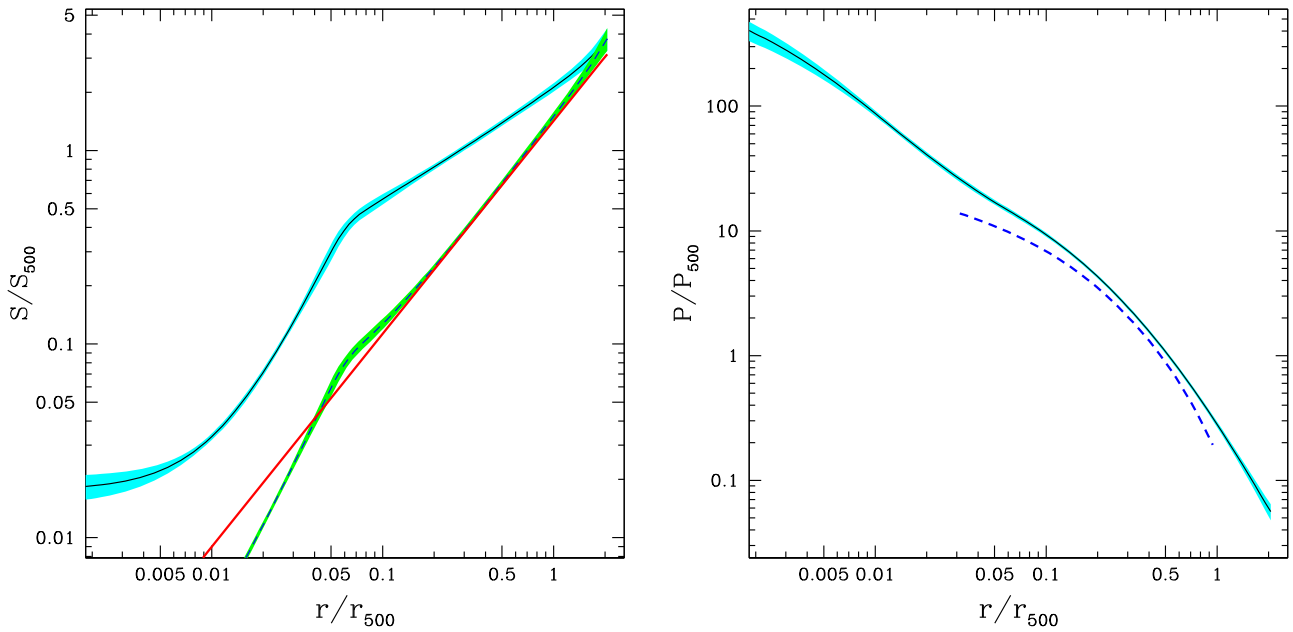

Figure 3. Left Panel: Radial entropy profile (black) and 1σ error region (cyan) for the fiducial hydrostatic model expressed in terms of the characteristic value S_{500}. The red line indicates the baseline $r^{1.1}$ profile produced by gravity-only cosmological simulations (Voit et al. 2005). The black dashed line (and green 1σ region) represents rescaling the entropy profile by a function of the gas fraction according to Pratt et al. (2010). Right Panel: pressure profile (black) compared to the universal profile inferred for groups and clusters by Arnaud et al. (2010), which is expected to apply for the radii shown.

Table 1
Pressure and Entropy

	$P_{\rm ref}$ (10^{-2} keV cm^{-3})	s_0 (keV cm^2)	s_1 (keV cm^2)	$r_{\rm b,1}$ (kpc)	$r_{\rm b,2}$ (kpc)	α_1	α_2	α_3
Best Fit	5.30 ± 0.25	4.48 ± 0.78	10.9 ± 1.3	35.6 ± 5.1	708 ± 277	1.81 ± 0.18	0.57 ± 0.06	1.01 ± 0.44
(Max Like)	(5.49)	(4.51)	(10.7)	(42.4)	(180)	(1.80)	(0.36)	(0.74)

Note. Constraints on the free parameters associated with the pressure and entropy for the fiducial hydrostatic model. $P_{\rm ref}$ is the normalization of the total thermal ICM pressure profile at the reference radius 10 kpc. The other parameters refer to the double broken power-law entropy model (Equation (3)). In the top row we list the marginalized "best-fitting" values and 1σ errors; i.e., the mean values and standard deviations of the parameters of the Bayesian posterior. In the second row we give the "maximum likelihood" parameter values that maximize the likelihood function.

pressure, $P_{500} = 5.9 \times 10^{-4}$ keV cm^{-3} (see Equation (5) of Arnaud et al. 2010), and compared it to the "universal" pressure profile of Arnaud et al. (2010). (Note that we quote results for the total gas pressure rather than the electron gas pressure and have accounted for this also in the definition of P_{500}.) In most of the region where the universal profile is expected to be valid, the pressure profile of RXJ 1159+5531 agrees within the 20% scatter in the pressure profiles of the clusters studied by Arnaud et al. (2010), reaching maximum deviations of 50%–60% at the endpoints; i.e., RXJ 1159+5531 has a pressure profile similar to the other clusters.

5.4. Mass

In Figure 4 we show the profiles for the total mass and different mass components for the fiducial hydrostatic model, while in Table 2 we list the results for $M_\star/L_K$ and the NFW parameters, concentration and mass, evaluated for several overdensities. Of all the mass components, the stellar mass has the weakest constraints ($\sim\pm18\%$), while the gas mass is the best constrained (e.g., $\sim\pm4\%$ at r_{108}.), considering only the statistical errors.

Most of the possible systematic errors we consider in Section 6, and listed in Table 2, are not significant since they induce parameter changes of the same size or smaller than the 1σ statistical error. The most significant changes result from aspects of the background modeling (Section 6.6), the treatment of the plasma emissivity (Section 6.8), and how the metal abundances are treated (Section 6.5), particularly in the outermost apertures; i.e., the CXBSLOPE, $\Lambda_\nu(T, Z)$, Solar Abun, and Fix $Z_{\rm Fe}(r_{\rm out})$ rows in Table 2. It is, however, reassuring that even these changes generally lead to parameter changes not much larger than 1σ. (See Section 6 for a more detailed discussion of the systematic error budget.)

The value we obtain for the K-band stellar mass-to-light ratio ($M_\star/L_K \approx 0.6 M_\odot/L_\odot$) of the BCG agrees very well with our previous determinations (Gastaldello et al. 2007; Humphrey et al. 2012a) and also is consistent with the value expected from stellar population synthesis models. Using the published relationship between stellar mass-to-light ratio and color from Zibetti et al. (2009), we obtain $M_\star/L_K \approx 0.55 M_\odot/L_\odot$ for $g - i = 1.41$, where the g and i magnitudes are taken from the "Model" entries in the NASA/IPAC Extragalactic Database (NED) referring to the Sloan Digital Sky Survey Data Release[5] 6. This good agreement should be considered only a mild consistency check, since (1) there is significant scatter depending on which bands are used for the color (we used

[5] http://www.sdss.org/dr6/products/catalogs/index.html

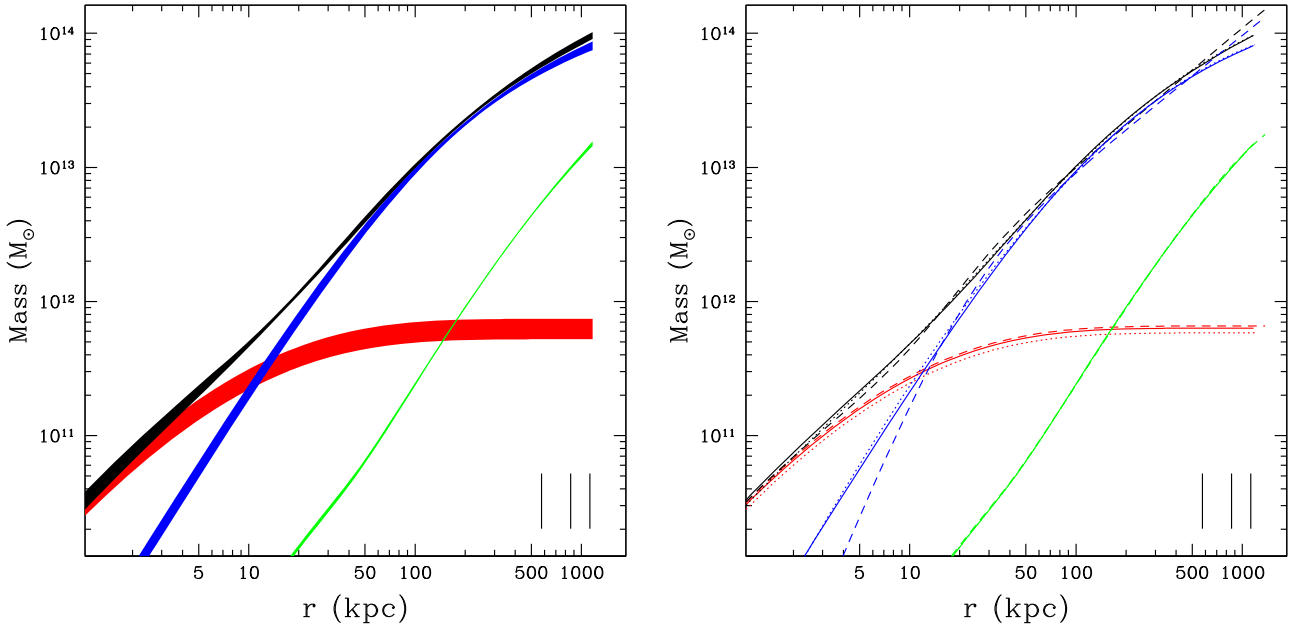

Figure 4. Left Panel: Radial profiles of the various mass components of the fiducial hydrostatic model: total mass (black), NFW DM (blue), stars (red), and hot gas (green). The vertical lines in the bottom right corner indicate the best-fitting virial radii for the fiducial model; i.e., from left to right: r_{500}, r_{200}, and r_{108}. Right Panel: Results shown for hydrostatic models having different dark matter profiles: NFW (solid lines), Einasto (dotted lines), and Corelog (dashed lines). Only the best-fitting models are shown. The color scheme is the same as for the left panel. The gas mass profiles are indistinguishable between the models.

Table 2
Stellar and Total Mass

	$M_\star/L_K$ $(M_\odot L_\odot^{-1})$	c_{2500}	M_{2500} $(10^{13}M_\odot)$	c_{500}	M_{500} $(10^{13}M_\odot)$	c_{200}	M_{200} $(10^{13}M_\odot)$	$c_{\rm vir}$	$M_{\rm vir}$ $(10^{13}M_\odot)$
Best Fit	0.61 ± 0.11	2.6 ± 0.4	3.1 ± 0.1	5.6 ± 0.7	5.9 ± 0.4	8.4 ± 1.0	7.9 ± 0.6	10.9 ± 1.3	9.4 ± 0.7
(Max Like)	(0.53)	(3.0)	(3.1)	(6.3)	(5.6)	(9.4)	(7.4)	(12.2)	(8.8)
Spherical	...	...	...	$^{+0.13}_{-0.32}$	$^{+0.15}_{-0.04}$	...	...	...	...
Einasto	−0.05	−0.2	−0.0	−0.4	0.1	−0.6	0.1	−0.9	0.1
CORELOG	−0.05	10.0	−0.4	23.1	0.5	37.5	2.4	51.7	4.7
1 Break	0.02	−0.1	0.0	−0.2	0.1	−0.2	0.2	−0.3	0.2
$\Lambda_\nu(T, Z)$	−0.04	0.2	−0.1	0.5	−0.4	0.7	−0.5	0.9	−0.6
Response	0.02	−0.2	0.0	−0.4	0.1	−0.6	0.3	−0.8	0.3
Proj. Limit	$^{+0.00}_{-0.00}$	$^{+0.0}_{-0.0}$	$^{+0.0}_{-0.0}$	$^{+0.0}_{-0.0}$	$^{+0.0}_{-0.0}$	$^{+0.1}_{-0.0}$	$^{+0.0}_{-0.0}$	$^{+0.1}_{-0.0}$	$^{+0.0}_{-0.0}$
SWCX	0.00	−0.0	0.0	−0.0	0.0	−0.1	0.1	−0.1	0.1
Distance	$^{+0.03}_{-0.02}$	$^{+0.1}_{-0.1}$	$^{+0.0}_{-0.0}$	$^{+0.1}_{-0.2}$	$^{+0.1}_{-0.1}$	$^{+0.2}_{-0.3}$	$^{+0.1}_{-0.1}$	$^{+0.2}_{-0.3}$	$^{+0.2}_{-0.2}$
$N_{\rm H}$	−0.02	0.1	−0.0	0.2	−0.1	0.3	−0.2	0.4	−0.3
Fix $Z_{\rm Fe}(r_{\rm out})$	$^{+0.05}_{-0.03}$	$^{+0.2}_{-0.3}$	$^{+0.2}_{-0.1}$	$^{+0.3}_{-0.5}$	$^{+0.5}_{-0.2}$	$^{+0.5}_{-0.8}$	$^{+0.7}_{-0.3}$	$^{+0.6}_{-1.1}$	$^{+0.8}_{-0.4}$
Solar Abun.	−0.05	0.3	−0.1	0.5	−0.3	0.7	−0.5	1.0	−0.6
PSF	0.03	−0.1	0.1	−0.3	0.2	−0.4	0.3	−0.5	0.4
FI–BI	0.02	−0.1	−0.0	−0.1	0.0	−0.2	0.1	−0.2	0.1
NXB	$^{+0.01}_{-0.00}$	−0.0	$^{+0.1}_{-0.0}$	−0.0	$^{+0.1}_{-0.0}$	−0.1	0.1	−0.1	$^{+0.1}_{-0.0}$
CXB	−0.01	0.0	0.0	0.1	−0.0	0.1	−0.0	0.1	−0.1
CXBSLOPE	$^{+0.06}_{-0.04}$	$^{+0.2}_{-0.4}$	$^{+0.3}_{-0.1}$	$^{+0.4}_{-0.7}$	$^{+0.8}_{-0.4}$	$^{+0.7}_{-1.0}$	$^{+1.1}_{-0.5}$	$^{+0.9}_{-1.4}$	$^{+1.2}_{-0.6}$

Notes. Best-fitting values, maximum likelihood values, and 1σ errors (see notes to Table 1) for the stellar mass-to-light ratio ($M_\star/L_K$), concentration, and enclosed mass corresponding to the total mass profile (stars+gas+DM) of the fiducial hydrostatic model computed for radii corresponding to several different overdensities. (Note: "vir" refers to $\Delta = 108$.) We also provide a detailed systematic error budget as explained in Section 6. For most of the entries we list the values using the same precision. If the particular error has a smaller value, it appears as a zero; e.g., "0.0" or "−0.0." Briefly, the systematic test names refer to tests of, ("Spherical," Section 6.1): the assumption of spherical symmetry; ("Einasto," "CORELOG," Section 6.4): using Einasto or CORELOG instead of NFW for the DM profile; ("1 Break," Section 6.3): only using one break radius for the entropy model; ("$\Lambda_\nu(T, Z)$," Section 6.8): different treatments for deprojecting the plasma emissivity; ("Response," Section 6.8): response weighting; ("Proj. Limit"), Section 6.8): outer radius of model cluster; ("SWCX," Section 6.6): Solar Wind Charge Exchange emission; ("Distance," Section 6.8): assumed distance; ("$N_{\rm H}$," 6.7): assumed Galactic hydrogen column density; ("Fix $Z_{\rm Fe}(r_{\rm out})$," Section 6.5)): effect of fixing the metal abundance in the outer *Suzaku* aperture to either $0.1Z_\odot$ or $0.3Z_\odot$; ("Solar Abun.," Section 6.5): using different solar abundance tables; ("PSF," Section 6.7): the sensitivity to the PSF mixing procedure for the *Suzaku* data; ("FI–BI," Section 6.7): the flux calibration of the different *Suzaku* CCDs; ("NXB," Section 6.6): the sensitivity to the adopted model of the non-X-ray background for the *Suzaku* data; ("CXB," Section 6.6): fixing the normalization of the CXB power law to the average value determined from surveys; and ("CXBSLOPE," Section 6.6): the sensitivity to the assumed slope in the CXB power la.

$g - i$ as favored by Zibetti et al. 2009), and (2) the relationship between color and $M_\star/L_K$ depends on the assumed stellar initial mass function (IMF). If instead we use the relationship between stellar mass-to-light ratio and color of Bell et al. (2003), who employ a Salpeter-like IMF, we obtain $M_\star/L_K \approx 0.94 M_\odot/L_\odot$, about 3σ above our measured value. While there is considerable scatter depending on the color used, the X-ray analysis favors the lower $M_\star/L_K$ obtained from Zibetti et al. (2009) who adopt a Milky Way IMF (Chabrier 2003). Several previous studies have found that massive early-type galaxies instead favor a Salpeter IMF (e.g., Conroy & van Dokkum 2012; Newman et al. 2013a; Dutton & Treu 2014), although the more recent study by, e.g., Smith et al. (2015) and most of our previous X-ray studies (e.g., Humphrey et al. 2009, 2012b) favor a Milky Way IMF.

Since fossil clusters like RXJ 1159+5531 are thought to be highly evolved, early forming systems, it is interesting to examine whether they possess large concentrations for their mass compared to the general population. According to the results of Dutton & Macciò (2014), the mean value of c_{200} for a "relaxed" DM halo with $M_{200} = 7.9 \times 10^{13}\, M_\odot$ in the *Planck* cosmology is 5.3, which is a little more than 3σ lower than the value we measure for RXJ 1159+5531 (8.4 ± 1.0). In addition, with respect to the intrinsic scatter of the theoretical relation, the c_{200} value is a $\sim 2\sigma$ outlier. Hence, with respect to the fiducial hydrostatic model with an NFW DM halo, RXJ 1159+5531 appears to possess a significantly above-average concentration, consistent with forming earlier than the average halo population. For the Einasto DM halo, our measured $c_{200} = 7.8 \pm 1.0$ is slightly more than 2σ above the mean predicted value of 5.6 and a little above the 1σ intrinsic scatter ($c_{200} = 7.5$) using the results of Dutton & Macciò (2014). The reduced significance for the Einasto case arises from a combination of our smaller measured c_{200} and also larger theoretical intrinsic scatter for the Einasto profile compared to NFW.

In the right panel of Figure 4 we compare the results for the different DM models. As is readily apparent from visual inspection, the gas mass profiles are virtually identical for all three cases; i.e., the inferred gas mass profile is robust to the assumed DM model. Over most of the radii investigated, the total mass profile is also quite insensitive to the assumed DM model, though CORELOG leads to a more massive halo than either NFW or Einasto. (Note in particular the "pinching" of the total mass profile near 10–20 kpc, about 1–2 R_e, where the DM crosses over the stellar mass.) The largest deviations appear at the very largest radii ($\gtrsim r_{108}$). The fitted stellar mass profile is very similar for all three DM models and yields consistent $M_\star/L_K$ values in each case.

All the DM models produce fits of similar quality in terms of the magnitude of their fractional residuals. When we perform a frequentist χ^2 fit we obtain minimum χ^2 values of 39.4 for Einasto, and 40.1 for CORELOG compared to 39.9 for NFW; i.e., the fits are statistically indistinguishable from the frequentist perspective. Moreover, from the Bayesian analysis we can use the ratio of evidences to compare the Einasto ($\log_{10} Z = -53.00$) and NFW ($\log_{10} Z = -53.81$) models since they have essentially the same free parameters and priors: We obtain an evidence ratio of 2.2 in favor of the Einasto model, which is not very significant. It is not straightforward to compare the evidences of the CORELOG and NFW models because they have different prior volumes (and the models are not "nested"). Nevertheless, the frequentist minimum χ^2 values clearly show that, despite the high-quality X-ray data covering the entire virial radius in projection, the data do not statistically disfavor the CORELOG model.

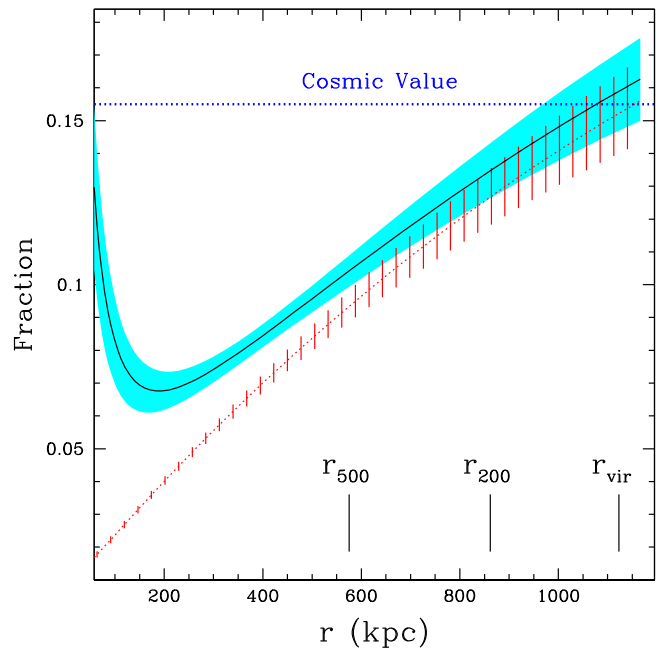

Figure 5. Radial profiles of the baryon (solid black line, cyan 1σ error region) and gas (dotted red line, red 1σ error region) fractions of the fiducial hydrostatic model.

For completeness, we have also examined allowing the Einasto index n to be a free parameter. Since, as just noted, the data are unable to distinguish clearly between the NFW, Einasto ($n = 5$), and CORELOG profiles (each of which have two free parameters), and these models already provide formally acceptable fits, it follows that adding another free parameter does not improve the fit very much. Indeed, for the frequentist fit we find that χ^2 is reduced by only 0.08 and gives a large 1σ error range on the index: $n = 5.8^{+4.6}_{-2.0}$ or $\alpha = 1/n = 0.17^{+0.09}_{-0.08}$. Despite the large uncertainty, the best-fitting Einasto index matches well the value expected for a DM halo of the mass of RXJ 1159+5531 (Dutton & Macciò 2014).

5.5. Gas and Baryon Fraction

The results for the baryon and gas fraction profiles using the fiducial hydrostatic model are displayed in Figure 5, and the parameter constraints are listed in Table 3 including the systematic error budget. Similar to the results for the total mass, most of the systematic errors are insignificant in the sense that the estimated parameter changes in the gas and baryon fraction are comparable to or less than the 1σ statistical error. Again, the most important changes occur for aspects of the background modeling (Section 6.6) and the treatment of the plasma emissivity (Section 6.8) and metal abundances (Section 6.5), particularly in the outermost apertures; i.e., the CXBSLOPE, $\Lambda_\nu(T, Z)$, Fix $Z_{\rm Fe}(r_{\rm out})$, and Solar Abun rows in Table 3. The CXBSLOPE and Fix $Z_{\rm Fe}(r)$ result in systematic errors almost 3σ in magnitude. (See Section 6 for a more detailed discussion of the systematic error budget.)

For most radii $f_{\rm b} < f_{\rm b,U}$, where $f_{\rm b,U} = 0.155$ is the mean baryon fraction of the universe as determined by *Planck*

Table 3
Gas and Baryon Fraction

	$f_{\rm gas,2500}$	$f_{\rm b,2500}$	$f_{\rm gas,500}$	$f_{\rm b,500}$	$f_{\rm gas,200}$	$f_{\rm b,200}$	$f_{\rm gas,vir}$	$f_{\rm b,vir}$
	0.051 ± 0.001	0.072 ± 0.004	0.093 ± 0.003	0.104 ± 0.004	0.126 ± 0.007	0.134 ± 0.007	0.152 ± 0.010	0.159 ± 0.010
(Max Like)	(0.052)	(0.070)	(0.093)	(0.103)	(0.127)	(0.134)	(0.155)	(0.161)
$M_{\rm stellar}^{\rm other}$	…	$^{+0.017}$	…	$^{+0.016}$	…	$^{+0.016}$	…	$^{+0.015}$
Spherical	…	…	$^{+0.0006}_{-0.0009}$	…	…	…	…	…
Einasto	−0.001	0.000	−0.002	−0.001	−0.002	−0.001	−0.002	−0.001
CORELOG	0.003	0.002	−0.003	−0.001	−0.018	−0.015	−0.037	−0.035
1 Break	0.000	−0.000	−0.001	−0.001	−0.001	−0.001	−0.000	−0.000
$\Lambda_\nu(T, Z)$	0.000	0.001	0.004	0.004	0.010	0.010	0.015	0.016
Response	0.001	0.001	−0.001	−0.001	−0.003	−0.003	−0.004	−0.004
Proj. Limit	$^{+0.000}_{-0.000}$	$^{+0.000}_{-0.000}$	$^{+0.000}_{-0.000}$	$^{+0.000}_{-0.000}$	$^{+0.001}_{-0.000}$	$^{+0.001}_{-0.000}$	$^{+0.001}_{-0.000}$	$^{+0.001}_{-0.000}$
SWCX	−0.000	−0.000	−0.000	−0.000	−0.000	−0.000	−0.000	−0.000
Distance	$^{+0.002}_{-0.001}$	$^{+0.001}_{-0.000}$	$^{+0.002}_{-0.001}$	$^{+0.002}_{-0.001}$	$^{+0.003}_{-0.002}$	$^{+0.003}_{-0.001}$	$^{+0.003}_{-0.002}$	$^{+0.002}_{-0.002}$
$N_{\rm H}$	−0.000	0.000	0.001	0.001	0.002	0.002	0.003	0.004
Fix $Z_{\rm Fe}(r_{\rm out})$	0.000	$^{+0.001}_{-0.000}$	$^{+0.003}_{-0.007}$	$^{+0.003}_{-0.007}$	$^{+0.006}_{-0.016}$	$^{+0.006}_{-0.016}$	$^{+0.009}_{-0.024}$	$^{+0.009}_{-0.024}$
Solar Abun.	−0.000	0.001	0.004	0.004	0.007	0.007	0.008	0.008
PSF	0.001	−0.000	−0.001	−0.002	−0.003	−0.003	−0.004	−0.004
FI–BI	0.002	0.001	0.003	0.003	0.005	0.005	0.007	0.007
NXB	$^{+0.001}_{-0.001}$	$^{+0.001}_{-0.000}$	$^{+0.002}_{-0.002}$	$^{+0.001}_{-0.002}$	$^{+0.001}_{-0.006}$	$^{+0.001}_{-0.005}$	$^{+0.000}_{-0.010}$	$^{+0.000}_{-0.010}$
CXB	−0.001	−0.000	−0.001	−0.001	−0.002	−0.002	−0.004	−0.004
CXBSLOPE	$^{+0.001}_{-0.001}$	$^{+0.001}_{-0.001}$	$^{+0.005}_{-0.009}$	$^{+0.005}_{-0.008}$	$^{+0.011}_{-0.018}$	$^{+0.011}_{-0.018}$	$^{+0.018}_{-0.027}$	$^{+0.018}_{-0.027}$

Note. Best-fitting values, maximum likelihood values, 1σ statistical errors, and estimated systematic errors (see notes to Table 1) for the gas and baryon fractions of the fiducial hydrostatic model computed for radii corresponding to several different overdensities. (Note: "vir" refers to $\Delta = 108$.)

(Planck Collaboration et al. 2014). Near r_{108}, $f_{\rm b}$ is consistent with $f_{\rm b,U}$, with the hot ICM consisting of 96% of the total baryons. These results are virtually identical to those for the Einasto model, where $f_{\rm b} = 0.157 \pm 0.011$ at r_{108}, whereas CORELOG has a smaller value, $f_{\rm b} = 0.121 \pm 0.008$.

The preceding discussion considered the baryons contained in the hot ICM and stellar baryons associated only with the BCG as determined by the fitted $M_\star/L_K$. To estimate the stellar baryons from non-central cluster members and ICL we follow the procedure we adopted in Section 4.3 of Humphrey et al. (2012a). Since the contribution of these non-BCG stellar baryons is not measured directly, we list it as a systematic error in Table 3 (see Section 6.2). At the largest radii these baryons are expected to increase the baryon fraction by ∼10%, which is not much larger than the statistical error at r_{108}.

5.6. Mass and Density Slopes

It is now well established that the total mass profiles of massive elliptical galaxies have density profiles very close to $\rho \sim r^{-\alpha}$ with $\alpha \approx 2$ over a wide range in radius. This relation extends to higher masses with smaller α in the central regions of clusters (e.g., Humphrey & Buote 2010; Newman et al. 2013b; Courteau et al. 2014; Cappellari et al. 2015 and references therein). In particular, in Humphrey & Buote (2010) it was shown that the total mass profiles inferred from hydrostatic studies of hot gas in massive elliptical galaxies, groups, and clusters, are fairly well approximated by a single power law over 0.2–10 stellar half-light radii (R_e) so that, approximately, $\alpha = 2.31 - 0.54\log(R_e/{\rm kpc})$, a result consistent with that obtained from combination of stellar dynamics and strong gravitational lensing for massive elliptical galaxies (Auger et al. 2010).

In Figure 6 we display the radial logarithmic derivatives (i.e., slopes) of the total mass and total density profiles for the fiducial hydrostatic model. The slopes are indeed slowly

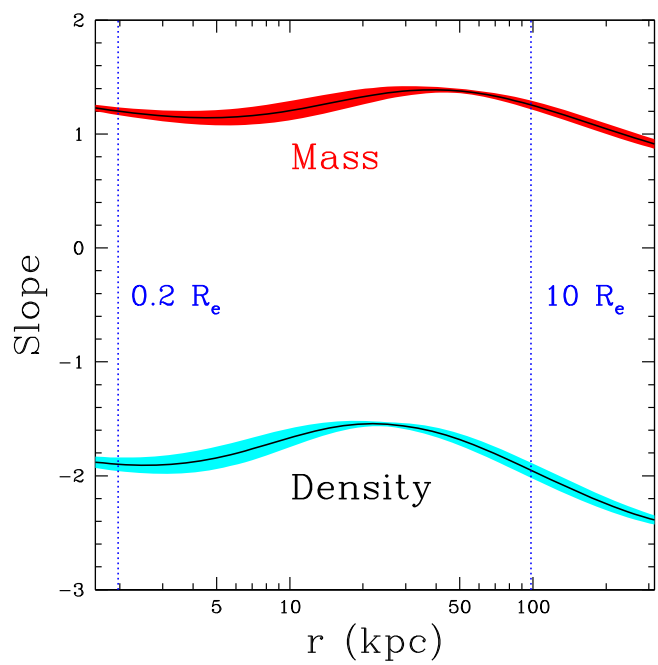

Figure 6. Slopes (i.e., logarithmic derivatives) of the total mass and total mass density for the fiducial hydrostatic model. The error regions shown are 1σ. The vertical lines indicate the regions between 0.2–10 stellar half-light radii (R_e) of the central galaxy that were studied in Humphrey & Buote (2010).

varying for our models, ranging from ≈1.2–1.4 for the mass to ≈−1.6 to −2.0 for the density over radii 0.2–10 R_e, representing a radial variation of ±20%. In Table 4 we quote the mass-weighted total density slope $\langle\alpha\rangle$ following Equation (2) of Dutton & Treu (2014),

$$\langle\alpha\rangle = 3 - \frac{d\ln M}{d\ln r},\ \alpha \equiv -\frac{d\ln\rho}{d\ln r}, \quad (4)$$

Table 4
Mass-weighted Total Density Slope

Radius (kpc)	Radius (R_e)	$\langle\alpha\rangle$
4.9	0.5	1.86 ± 0.07
9.8	1.0	1.80 ± 0.08
19.7	2.0	1.67 ± 0.07
49.2	5.0	1.62 ± 0.02
98.3	10.0	1.74 ± 0.04

Note. The mass-weighted slope is computed for the fiducial hydrostatic model with Equation (4).

where M is the total mass enclosed within radius r. Within $10R_e$, $\langle\alpha\rangle = 1.74 \pm 0.04$, which is consistent with the value of $\alpha = 1.67^{+0.11}_{-0.10}$ we obtained previously from a power-law fit to the mass profile (Humphrey & Buote 2010) and with $\alpha = 1.77$ obtained using the $\alpha - R_e$ scaling relation.

5.7. MOND

While the presence of DM is largely accepted by the astronomical community, it is worthwhile to examine interpretations of the observations that instead consider a modification of the gravitational force law. Here we consider the most widely investigated and successful modified gravity theory, MOND (Milgrom 1983), which nevertheless is unable to explain observations of galaxy clusters considering only the known baryonic matter (e.g., Sanders 1999; Pointecouteau & Silk 2005; Angus et al. 2008; Milgrom 2015). We investigate whether MOND can obviate the need for DM in RXJ 1159 +5531 following the approach of Angus et al. (2008).

For an isolated spherical system the gravitational acceleration in Newton gravity, $g_{\rm N} = GM_{\rm N}(<r)/r^2$, and MOND, $g_{\rm M} = GM_{\rm M}(<r)/r^2$, have similar forms, where $M_{\rm N}(<r)$ and $M_{\rm M}(<r)$ are the respective enclosed masses within radius r. For some interpolating function, $\mu(g_{\rm N}/a_0)$, the accelerations are related by $g_{\rm M} = \mu(g_{\rm N}/a_0)g_{\rm N}$, so that $M_{\rm M} = \mu(g_{\rm N}/a_0)M_{\rm N}$, and $a_0 \approx 1.2 \times 10^{-8}$ cm s^{-2} is the MOND acceleration constant. For $\mu(x) = x/(1 + x)$, where $x = g_{\rm N}/a_0$, we have

$$M_{\rm M}(<r) = \frac{M_{\rm N}(<r)}{1 + a_0/g_{\rm N}(r)}. \quad (5)$$

In this way we easily compute the MONDian mass using the Newtonian mass we have derived previously; i.e., there is no different fitting required. Equation (5), being derived from the simple interpolating function μ, has the undesirable property that $M_{\rm M}(<r)$ reaches a maximum value at some radius and then decreases (for more discussion of this point see Angus et al. 2008). Hence, for the moment we focus on results roughly within the radius where the MONDian mass reaches a maximum value.

In Figure 7 for the fiducial hydrostatic model we compare the cumulative DM fractions ($M_{\rm DM}/M_{\rm total}$) inferred from Newtonian gravity and MOND. As in the Newtonian case, MOND requires a dominant fraction of DM with increasing radius to match the X-ray data. At $r = 100$ kpc the DM fraction is 85.0% ± 2.5%; i.e., the mass discrepancy is a factor of 6.7. Even when considering the contribution of baryons from (rather uncertain) non-central baryons (Section 6.2), the DM fraction is reduced by only a small amount to ≈82%.

It is also interesting to view the performance of MOND from a different perspective. Solving the MOND equation for $g_{\rm N}$ with the same interpolating function yields

$$g_{\rm N} = \frac{g_{\rm M}}{2}\left(1 + \sqrt{1 + 4\frac{a_0}{g_{\rm M}}}\right). \quad (6)$$

That is, given $g_{\rm M}$ evaluated using the baryonic mass profiles (i.e., stellar and gas) derived from the Newtonian analysis, this expression gives $g_{\rm N}$, and thus the Newtonian mass profile (with DM) that MOND would predict. In Figure 7 we compare this "MOND-predicted Newtonian mass profile" with the actual Newtonian total mass profile. The MOND profile underpredicts the Newtonian mass over most radii, with the largest deficit again occurring near $r = 100$ kpc such that the predicted mass is $\approx 0.30M_{\rm N}$. The predicted profile crosses over the Newtonian profile shortly before r_{200} and then exceeds the Newtonian profile afterwards.

In sum, consistent with previous results for X-ray groups and clusters, MOND requires a large fraction of DM similar to Newtonian gravity to explain the X-ray data.

5.8. Comparison to Previous Work

It is interesting to compare our results to those obtained by Humphrey et al. (2012a) who used only the *Chandra* data and the North *Suzaku* observation. Humphrey et al. (2012a) obtained best-fitting values, $M_\star/L_K = 0.54$ (in solar units), $c_{\rm vir} = 11.2$, $M_{\rm vir} = 9.3 \times 10^{13}\,M_\odot$, and $f_{\rm b,500} = 0.124$ (includes non-BCG stellar baryons). All of these results agree within 1σ of the values obtained in our study (Tables 2 and 3).

The excellent agreement between the two studies is notable for several reasons. First, the addition of the *Suzaku* observations covering out to r_{200} in the S, E, and W directions does not modify the results significantly, consistent with the results of Paper 1, indicating only small azimuthal variation in the ICM properties at large radius. Second, improved background modeling incorporating point sources resolved by offset *Chandra* observations—as well as improved calibration and data processing in the *Chandra* and *Suzaku* pipelines—does not change the results significantly. Finally, the consistent results between the studies provide a useful consistency check on the different implementations of the entropy-based hydrostatic modeling (e.g., treatment of self-gravity of gas mass; see Section 3) between the two studies using entirely different modeling software.

6. ERROR BUDGET

We have considered a variety of possible sources of systematic error and list a detailed error budget in Tables 2 and 3. Below we provide details on the construction of the error budgets.

6.1. Spherical Symmetry

Buote & Humphrey (2012b) showed that assuming a cluster is spherical when in fact it is ellipsoidal does not typically introduce large errors into the quantities inferred from hydrostatic modeling of the ICM. For a large range of intrinsic flattenings, they computed orientation-averaged biases (mean

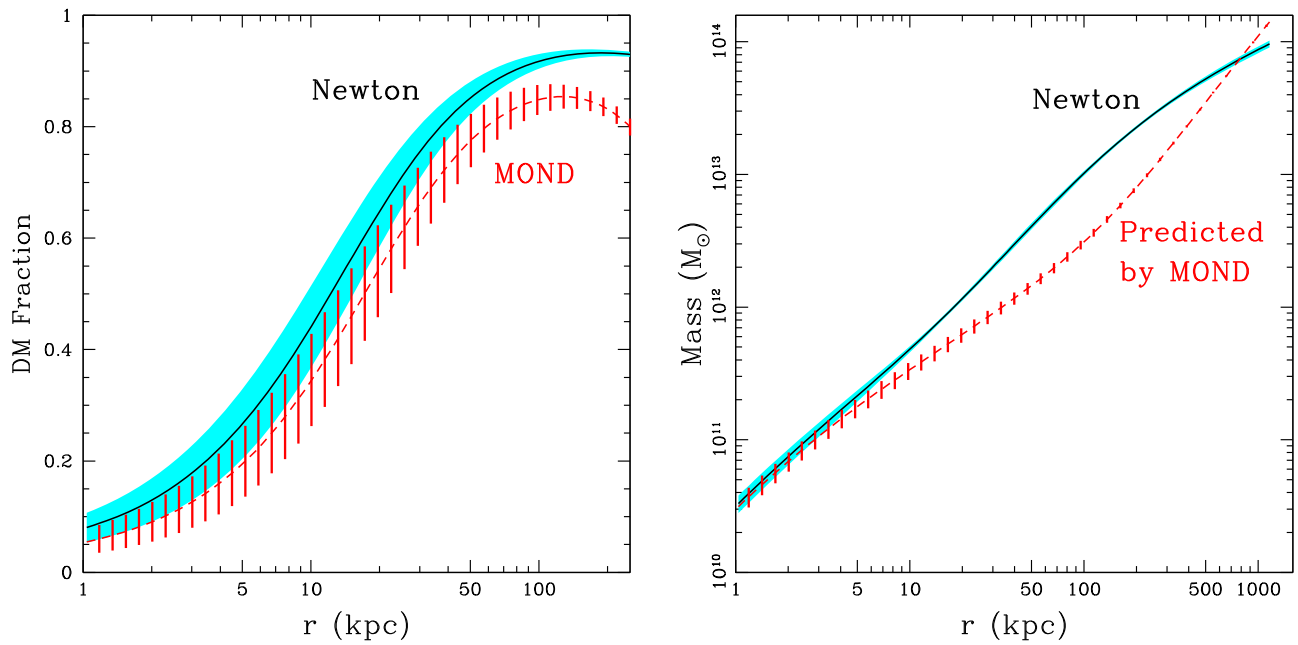

Figure 7. Left Panel: Radial profiles of the DM fraction for the fiducial hydrostatic model for the Newtonian (black and cyan) and MOND (red) cases. The shaded and hashed regions represent 1σ errors. Right Panel: newtonian mass profiles for (1) the total mass of the fiducial hydrostatic model (black and cyan, same as in Figure 4), and (2) the total mass profile predicted by MOND (red) from Equation (6).

values and scatter) of several derived quantities, including halo concentration, total mass, and gas fraction.

We use the "NFW-EMD" results from Table 1 of Buote & Humphrey (2012b) to provide an estimate of the error arising from the assumption of spherical symmetry within r_{500}; i.e., the error from assuming that the cluster is spherical when in fact it is a flattened ellipsoid viewed at a random orientation to the line of sight. From a study of cosmological DM halos Schneider et al. (2012) find that for a halo having mass similar to RXJ 1159+5531 the typical intrinsic short-to-long axis ratio is ≈0.5. We adopted this value for the error estimates on the concentration, mass, and gas fraction within r_{500} in Tables 2 and 3 ("Spherical"). In all cases the effect is insignificant.

6.2. Stellar Mass

While the BCG dominates the stellar mass in the central region of the cluster, smaller non-central galaxies and diffuse ICL contribute significant stellar mass at larger radius. Due to the greater uncertainty of the amounts and distributions of these non-central baryons, we treat their contribution as a systematic effect to the baryon fraction. To account for these additional stellar baryons, we follow the procedure described in Section 4.3 of Humphrey et al. (2012a). For the non-central galaxies we use the result of Vikhlinin et al. (1999) that these galaxies comprise ∼25% of the V-band stellar light. We assume that this result also applies in the K-band with the same $M_\star/L_K$ as the BCG. Since we do not have a precise observational constraint on the ICL, we use the result from the theoretical study by Purcell et al. (2007) that the ICL contains up to ∼2 times the stellar mass of the BCG and adopt this value to give a conservative reflection of the systematic error. We assume that both components of non-central baryons are spatially distributed as the DM in our models.

The contribution of the non-central baryons to the baryon fraction are listed in Table 3 ($M_{\rm stellar}^{\rm other}$). These stellar baryons increase $f_{\rm b,vir}$ by ∼10% to 0.174, fully consistent with the value reported in Humphrey et al. (2012a) containing the contributions from both the BCG and non-central stellar baryons. This modified $f_{\rm b,vir}$ exceeds the cosmic value $f_{\rm b,U} = 0.155$ by 2σ considering only the statistical error on our fiducial model, although the disagreement should be considered less significant given the uncertainties in the non-central stellar baryons.

6.3. Entropy Model

We examined the effect of restricting the entropy broken power-law model to only a single break (ONEBREAK). The effect is everywhere insignificant.

6.4. DM Model

The effects of using a DM profile different from NFW are indicated in the rows "Einasto" and "Corelog" in Tables 2 and 3. We have discussed the magnitudes of these systematic differences in Sections 5.4 and 5.5.

6.5. Metal Abundances

We considered how choices made in the measurement of the metal abundances from the spectral fitting affected the results. (We refer the reader to Paper 1 for details on the spectral analysis.) First, we examined the impact of using different solar reference abundances. Whereas our default analysis used the solar abundance table of Asplund et al. (2006), the effects of instead using the tables of Anders & Grevesse (1989) or Lodders (2003) are listed in the "Solar Abun" row in Tables 2 and 3. The differences do not exceed the 1σ statistical error.

Second, since the spectra in the outermost apertures (i.e., at the virial radius) are the most background dominated and subject to systematic errors, we also examined the impact of fixing the metal abundance there at $0.1Z_\odot$ and $0.3Z_\odot$, bracketing the best-fitting value of $\sim 0.2Z_\odot$ (referred to as "Δabun" in Table 3 of Paper 1). As can be seen in the row "Fix $Z_{\rm Fe}(r_{\rm out})$" in Tables 2 and 3, this effect leads to one of the two

largest systematic errors as mentioned above in Sections 5.4 and 5.5.

6.6. Background

We considered the impact of several choices made in the treatment of the background in the spectral fitting (see Paper 1). The effect of including a model for the solar wind charge exchange emission in the spectral analysis is listed in row "SWCX" in Tables 2 and 3. We find the effect to be insignificant in all cases.

To assess the sensitivity of the results to the particle background in the *Suzaku* observations, we artificially increased and decreased the estimated non-X–ray background component by ±5% and list the results in row "NXB" in Tables 2 and 3. In all instances the differences are insignificant for the stellar and total mass parameters. While this is also true at most radii for the gas and baryon fractions, at $r_{\rm vir}$ the differences are comparable to the 1σ error.

We also explored the sensitivity of our results to the extragalactic cosmic X-ray background (CXB) power-law component (see Section 5.1 of Paper 1). In Paper 1 by default we assumed a power-law component in our spectral fits with a slope fixed at $\Gamma = 1.41$ (e.g., De Luca & Molendi 2004) and normalization free to vary. If we fix the normalization to the value expected for the cosmic average (see Section 2.3 of Paper 1), we obtain the results listed in row "CXB" in Tables 2 and 3. It is reassuring that the differences are all negligible. If instead we keep the normalization free to vary but change the slopes used to $\Gamma = 1.3$, 1.5, we obtain the results listed in row "CXBSLOPE" (corresponding to "CXB-Γ" in Table 3 of Paper 1). As already noted in Sections 5.4 and 5.5, this effect leads to one of the two largest systematic errors. The differences are comparable to the 1σ errors within r_{2500} and increase to 2–3σ at $r_{\rm vir}$, where the data are most dominated by the background.

6.7. Miscellaneous Spectral Fitting

We performed other tests associated with the spectral fitting that we summarize here. In all cases they did not produce significant parameter differences in Tables 2 and 3. (1) The effect of varying the adopted value of Galactic $N_{\rm H}$ (Dickey & Lockman 1990) by ±20% is shown in row "$N_{\rm H}$" in Tables 2 and 3 (see Section 5.6 of Paper 1). (2) We varied the spectral mixing between extraction annuli by ±5% from our default case to assess the impact of small changes on how we account for the large, energy-dependent *Suzaku* PSF (see Section 5.3 of Paper 1). The results are given in row "PSF" in Tables 2 and 3. (3) By default we allowed the normalization of the ICM model for annuli on the *Suzaku*/XIS front-illuminated (FI) and back-illuminated (BI) chips to be varied separately to allow for any calibration differences. To assess the impact of this choice, we also performed the spectral fitting requiring the same normalizations for the FI and BI chips (Section 5.7 of Paper 1), and the results are given in the "FI–BI" row in Tables 2 and 3.

6.8. Miscellaneous Hydrostatic Modeling

Here we describe a few remaining tests we performed associated with choices made in our hydrostatic modeling procedure. First, we varied the cluster redshift by ±5% in our hydrostatic models (it was similarly varied in the spectral fitting in Paper 1), and the results are listed in the "Distance" row of Tables 2 and 3. The differences are everywhere insignificant. Second, we explored the impact of changing the default bounding radius of the cluster model. Whereas the default employed is 2.5 Mpc, in the "Proj. Limit" row of Tables 2 and 3 we show the differences resulting from instead using either 2.0 Mpc or 3.0 Mpc for the bounding radius. In all cases the effect is negligible. Next we examined the sensitivity of the results to the "response weighting" (Section 3) by instead performing no such weighting. As indicated in the "Response" row of Tables 2 and 3 the differences are insignificant.

Finally, we examined how our choices regarding the modeling of the plasma emissivity affect the results. As discussed in Section 3, the hydrostatic models by default take the measured metal abundance profile in projection and assigns it to be the true three-dimensional profile, which is then used (along with the temperature) to compute the plasma emissivity $\Lambda_\nu(T, Z)$. Our default procedure to do this assignment uses the *Chandra* data and only the N *Suzaku* observation. We investigated using instead each of the other three *Suzaku* pointings. For a more rigorous test, we also fitted a projected, emission-weighted parametric model to the projected iron abundance profile (Figure 13 of Paper 1). We employed a multi-component model consisting of two power laws mediated by an exponential (Equation (5) of Gastaldello et al. 2007) and a constant floor of $0.05Z_\odot$. The results of both of these tests for the plasma emissivity are listed in row "$\Lambda_\nu(T, Z)$" of Tables 2 and 3. The differences are among the largest, though in most cases are less than the 1σ error. In detail, both the metallicity model test and the cases where the E and S *Suzaku* pointings are used produce negligible results. The differences indicated in the tables are largest when the W *Suzaku* pointing is used to assign the metallicity profile.

7. DISCUSSION

7.1. Distinct Stellar BCG and DM Halo Components

Previously in Zappacosta et al. (2006) we made the observation that in massive galaxy clusters (i.e., with virial mass larger than a few $10^{14}\,M_\odot$) the total gravitating mass profile inferred from X-ray studies is itself generally well described by a single NFW profile without any need for a distinct component for stellar mass from the central BCG. On the other hand, individual massive elliptical galaxies (e.g., Humphrey et al. 2006, 2011, 2012b) and group-scale systems (e.g., Gastaldello et al. 2007; Zhang et al. 2007; Démoclès et al. 2010; Su et al. 2014) with virial masses less than $10^{14}\,M_\odot$ studied with X-rays usually (but do not always) require distinct stellar BCG and DM mass components.

The most massive clusters where X-ray observations clearly require distinct stellar BCG (with a reasonable stellar mass-to-light ratio) and DM (without an anomalously low concentration) mass components are RXJ 1159+5531 ($M_{200} = 7.9 \pm 0.6 \times 10^{13}\,M_\odot$) and A262 ($M_{200} = 9.3 \pm 0.8 \times 10^{13}\,M_\odot$, Gastaldello et al. 2007). Hence, from the perspective of X-ray studies, $\sim 10^{14}\,M_\odot$ appears to represent a point of demarcation above which the total mass profile, rather than the DM profile, is represented by a single NFW component.

Since X-ray images of the central regions of cool core clusters typically display irregular features (e.g., cavities) believed to be associated with intermittent AGN feedback, it is tempting to speculate that the inability to detect a distinct

stellar BCG component in massive cool core clusters reflects simply a strong violation of the approximation of hydrostatic equilibrium used to measure the mass profile. However, Newman and colleagues (Newman et al. 2013b) have used a combination of stellar dynamics and gravitational lensing to perform detailed studies of the radial mass profiles in several galaxy clusters. In their most recent study of 10 clusters (Newman et al. 2015), they also propose $\sim 10^{14}\,M_\odot$ as the mass above which the total mass profile, rather than the DM, is well described by a single NFW component.

The consistent picture obtained by X-ray, stellar dynamics, and lensing studies provides strong evidence for the reality of this transition mass. This has important implications for models of cluster formation since $\sim 10^{14}\,M_\odot$ appears to represent the mass scale where dissipative processes become important in the formation of the central regions of galaxy groups and clusters; i.e., above this mass the impact of dissipative processes on the total mass profile has been counteracted by late-time collisionless merging that re-establishes the NFW profile (e.g., Loeb & Peebles 2003; Laporte & White 2015).

As discussed in Section 5.6, the various mass components of RXJ 1159+5531 combine to produce a nearly power-law total mass profile with slowly varying logarithmic density slope ranging between $\alpha \approx -1.6$ to -2.0 within a radius $\sim$100 kpc ($\sim 10R_e$). This result is not strongly dependent on the assumed DM profile (NFW, Einasto, CORELOG). The slope α is consistent with that inferred from the scaling relation with R_e proposed by Humphrey & Buote (2010) and Auger et al. (2010).

This nearly power-law behavior in the total mass obeying scaling relations between α and R_e (and stellar density) for early-type galaxies is known as the "Bulge-Halo Conspiracy." Using empirically constrained ΛCDM models Dutton & Treu (2014) argue that a complex balance between feedback and baryonic cooling is required to explain this "conspiracy."

7.2. High DM Concentration

While some early X-ray studies indicated that fossil groups and clusters have unusually large NFW DM concentrations, essentially all of those measurements were inflated by neglecting to include the stellar BCG component in the mass modeling (e.g., Mamon & Lokas 2005). For the fossil cluster RX J1416.4 + 2315, Khosroshahi et al. (2006) accounted for the presence of the stellar BCG component and inferred a DM concentration of $c_{200} = 11.2 \pm 4.5$, which is about 2σ above the value of $\sim$4 expected for a relaxed halo with $M_{200} = 3.1 \times 10^{14}\,M_\odot$ according to Dutton & Macciò (2014). The result we obtained for RXJ 1159+5531 in Section 5.4 is a 3σ discrepancy, providing even stronger evidence for an above-average concentration in a fossil cluster, suggestive of a halo that formed earlier than the general population. (We note that we have not included adiabatic contraction (e.g., Blumenthal et al. 1986; Gnedin et al. 2004) of the DM halo in our model, which would lead to an even larger concentration.) We caution, however, that as noted in Section 5.4, when the Einasto DM model is employed the significance of RXJ 1159+5531 as an outlier is somewhat reduced.

It is also worth emphasizing that from the perspective of relaxed, low-redshift X-ray clusters, the concentration of RXJ 1159+5531 is not very remarkable. The only study that has measured the X-ray concentration-mass relation for a sizable number of relaxed systems having masses both lower and higher than RXJ 1159+5531 is Buote et al. (2007), which also included the measurement of RXJ 1159+5531 by Gastaldello et al. (2007). Our value for RXJ 1159+5531 is only $\sim 1\sigma$ larger than the mean relation obtained by Buote et al. (2007). The higher normalization of the X-ray concentration-mass relation can be explained by including reasonable star formation and feedback in the cluster simulations (Rasia et al. 2013) ,which are not present in the DM-only simulations of Dutton & Macciò (2014).

7.3. Gas Fraction

Recently, Eckert et al. (2015) have used gas masses inferred from *XMM-Newton* and total masses from weak lensing to measure gas fractions at r_{500} for a large cluster sample. They conclude that the gas fractions measured in this way are significantly smaller than those obtained from hydrostatic studies (e.g., Ettori 2015). By assuming that the weak-lensing masses are accurate, Eckert et al. (2015) infer a hydrostatic mass bias of $0.72^{+0.08}_{-0.07}$. When compared to numerical hydrodynamical simulations (Le Brun et al. 2014), the small gas fractions obtained by Eckert et al. (2015) favor an extreme feedback model in which a substantial amount of baryons are ejected from cluster cores.

From our hydrostatic analysis of RXJ 1159+5531 we measured within a radius r_{500}: $M_{500} = (5.9 \pm 0.4) \times 10^{13}\,M_\odot$ and $f_{\rm gas} = 0.093 \pm 0.003$ (Tables 2 and 3). For this value of M_{500}, the best-fitting relation for the gas fraction obtained by Eckert et al. (2015) gives $f_{\rm gas} = 0.05$, implying a hydrostatic mass bias of $\approx$80%. Since the wealth of evidence indicates that the ICM in RXJ 1159+5531 is very relaxed (see below in Section 7.4), including that the value of $f_{\rm gas} \approx 0.09$ we measure agrees much better with the cluster gas fractions produced in the simulations of Le Brun et al. (2014) considering plausible cooling and supernova feedback, we do not believe that such a large hydrostatic mass bias in RXJ 1159+5531 is supported by the present observations. Instead, we believe that these results for RXJ 1159+5531 support the suggestion by Eckert et al. (2015) that the weak lensing masses are biased high.

7.4. Hydrostatic Equilibrium Approximation

As we have noted previously in the related context of elliptical galaxies (see Section 8.2.2.1 of Buote & Humphrey 2012a), even without possessing direct, precise measurements of the hot gas kinematics, it is still possible to identify relaxed systems where the hydrostatic equilibrium approximation should be most accurate. RXJ 1159+5531 is a cool core cluster and displays a very regular X-ray image from the smallest scales probed by *Chandra* (with little or no evidence for AGN-induced disturbances) out to r_{200}. The *Suzaku* images mapping the radial region from $\sim r_{2500} - r_{200}$ with full azimuthal coverage display remarkably homogeneous ICM properties (Paper 1).

We are able to obtain a good representation of the X-ray data with hydrostatic models with reasonable values for the model parameters: (1) the stellar mass-to-light ratio is consistent with stellar population synthesis models (Section 5.4); (2) the value of the concentration, while statistically higher than the expected mean of the halo population, is within the 2σ cosmological intrinsic scatter (Section 5.4), and, at any rate, deviations from

hydrostatic equilibrium due to additional non-thermal pressure support should tend to produce anomalously low, not high, concentrations by leading to smaller inferences of the virial mass and radius (e.g., see discussion in Section 6.2 of Buote et al. 2007); and (3) the baryon fraction is consistent with the cosmic value.

Although it is tempting to ascribe the very relaxed state of RXJ 1159+5531 to it being a fossil cluster, recent evidence suggests that the X-ray properties of fossil systems are not significantly distinguishable from the general cluster population (Girardi et al. 2014). The apparently highly relaxed ICM within r_{200} implies that non-thermal pressure support is small throughout the cluster and, as such, constrains theories that predict a large amount of non-thermal pressure support from the magneto-thermal instability in the ICM outside of r_{500} (e.g., Parrish et al. 2012).

8. CONCLUSIONS

We present a detailed hydrostatic analysis of the ICM of the fossil cluster RXJ 1159+5531, a system especially well suited for study of its mass distribution with current X-ray observations. At a redshift of 0.081 it is sufficiently distant to allow mapping of its entire virial region on the sky with reasonable exposures, while still being close enough to spatially resolve the central regions near the BCG. Previous studies have shown this cluster to have a remarkably regular and undisturbed ICM (Vikhlinin et al. 1999, 2006; Gastaldello et al. 2007; Humphrey et al. 2012a). In Paper 1 we presented three new *Suzaku* observations in the south, east, and west directions, which, in conjunction with the existing *Suzaku* pointing to the north and central *Chandra* data, allow complete azimuthal and radial coverage on the sky within r_{200}. Our separate analysis of the ICM in each of the four directions found the ICM properties to be very homogenous in azimuth, testifying to the relaxed state of the ICM out to r_{200} (see Paper 1).

We constructed hydrostatic models and fitted them simultaneously to the projected ICM temperature and emission measure ($\propto \rho_{\rm gas}^2$) measured individually for each *Chandra* and *Suzaku* observation (see Paper 1). We employ an "entropy-based" procedure (Humphrey et al. 2008; Buote & Humphrey 2012a) where the hydrostatic equilibrium equation is expressed in terms of the entropy proxy S and total mass, which allows the additional contraint of convective stability ($dS/dr > 0$) to be easily enforced. Our fiducial model consists of a power law with two breaks and a constant for S, a Sérsic model for the stellar mass of the BCG, and an NFW DM halo. We explore the parameter space and determine confidence limits using a Bayesian Monte Carlo procedure and find that the fiducial model is a good fit to the data.

We constructed a detailed budget of systematic errors (Section 6) to assess the impact that different data analysis and modeling choices have on our measurements. The largest systematic effects are associated with the background spectral models, metal abundances, and modeling the plasma emissivity variation with radius. These effects are most significant at the largest radii, although none of them change qualitatively the results of the fiducial model.

The principal results are the following:

1. *Entropy.* The radial entropy profile of the ICM is described well by the power-law model with either one or two breaks. When rescaled in terms of the "virial" entropy (S_{500}), the entropy exceeds the $\sim r^{1.1}$ profile predicted by pure gravitational formation until $\sim r_{200}$, but does not fall below it at any radius. Further rescaling of the entropy by $(f_{\rm gas}/f_{\rm b,U})^{2/3}$ matches very well the $\sim r^{1.1}$ profile, suggesting that feedback has spatially redistributed the ICM rather than raised its temperature (Pratt et al. 2010).
2. *Pressure.* The radial pressure profile expressed in terms of P_{500} slightly exceeds the mean "universal" pressure profile of Arnaud et al. (2010), but is consistent within the scatter of that profile.
3. *BCG Stellar Mass and Dissipation Scale.* The stellar mass of the BCG is clearly required by the model fits and yields a K-band stellar mass-to-light ratio, $M_\star/L_K = 0.61 \pm 0.11\ M_\odot/L_\odot$, consistent with stellar population synthesis models for a Milky Way IMF. This makes RXJ 1159+5531 along with A262 (Gastaldello et al. 2007) the most massive clusters where X-ray studies have measured such a distinct BCG stellar component and supports recent work (Laporte & White 2015; Newman et al. 2015), suggesting that $\sim 10^{14}\ M_\odot$ represents the mass scale above which dissipation does not dominate the formation of the inner regions of clusters (Section 7.1).
4. *DM Profiles.* Despite the high-quality X-ray data covering the entire region within r_{200}, our model fits do not statistically distinguish between NFW, Einasto ($n = 5$), or CORELOG (singular isothermal sphere with a core) profiles for the DM halo. This contrasts with clusters much more massive than RXJ 1159+5531 where previous X-ray studies (e.g. Pointecouteau et al. 2005) clearly disfavor pseudo-isothermal models in favor of NFW, which is also found by recent results from the CLASH survey from gravitational lensing analysis of several very massive clusters (Umetsu et al. 2015). Allowing the Einasto index n to be free does not improve the fit significantly and yields $n = 5.8^{+4.6}_{-2.0}$ or $\alpha = 1/n = 0.17^{+0.09}_{-0.08}$, very consistent with the values expected for a DM halo of the mass of RXJ 1159+5531 (Dutton & Macciò 2014).
5. *High Concentration.* For the fiducial model (i.e., with an NFW profile) we obtain $c_{200} = 8.4 \pm 1.0$ and $M_{200} = (7.9 \pm 0.6) \times 10^{13}\ M_\odot$. The concentration exceeds the value of 5.2 expected for the mean relaxed cluster population in the Planck cosmology (Dutton & Macciò 2014) by 3σ. It is also a $\sim 2\sigma$ outlier considering the intrinsic scatter of the theoretical relation, although the discrepancy is reduced to a little more than a 1σ outlier when the Einasto DM profile is used. These properties make RXJ 1159+5531 the most significant overconcentrated fossil cluster to date (see Section 7.2), indicating an earlier formation time than the average cluster at its redshift. However, with respect to a sample of relaxed, low-redshift galaxy systems studied in X-rays spanning a mass range of $\sim 10^{12}$–$10^{15}\ M_\odot$, the concentration of RXJ 1159+5531 is only $\sim 1\sigma$ above the mean relation of Buote et al. (2007).
6. *Gas and Baryon Fraction.* Considering only the baryons associated with the ICM and the BCG, we obtain a baryon fraction at r_{200}, $f_{\rm b,200} = 0.134 \pm 0.007$, that is slightly below the Planck value (0.155) for the universe, but the baryon fraction continues to rise with radius so

that, $f_{\rm b,vir} = 0.159 \pm 0.010$ at $r_{\rm vir} = r_{108}$. Taking into account estimates for the stellar baryons associated with non-central galaxies and ICL increases these values by $\approx$0.015, in which case $f_{\rm b,vir}$ marginally exceeds (by 2σ) the cosmic value. Since our estimate of the ICL mass is very uncertain, we do not consider the disagreement to be significant; i.e., the baryon fraction is consistent with the cosmic value and therefore no significant baryon loss from the system.

7. *Slope of the Total Mass Profile.* The total mass profile is nearly a power law over radii 0.2–10R_e with a slope ranging from $\approx$1.2–1.4 and density slope α ranging from -1.6 to -2.0. Within 10$R_{\rm e}$, the mass-weighted slope of the total density profile, $\langle\alpha\rangle = 1.74 \pm 0.04$, is consistent with the value $\alpha = 1.77$ obtained using the $\alpha - R_e$ scaling relation (Auger et al. 2010; Humphrey & Buote 2010).
8. *MOND.* Following the procedure of Angus et al. (2008) using a particular simple interpolating function $\mu(g_{\rm N}/a_0)$, we computed mass profiles in the context of MOND. We find that MOND requires DM fractions nearly as large as for conventional Newton gravity: At $r = 100$ kpc the DM fraction is 85.0% $\pm$ 2.5%, implying a mass discrepancy of a factor of 6.7. The DM fraction decreases to $\approx$82% considering the (rather uncertain) contribution of non-central stellar baryons (Section 6.2). Therefore, consistent with previous results for other X-ray groups and clusters, MOND requires a large DM fraction to explain the X-ray data.

In sum, our hydrostatic analysis of the ICM emission within r_{200} yields baryon and DM properties quite consistent with typical clusters for its virial mass in the ΛCDM paradigm. The only notable exception is the higher-than-average NFW concentration parameter that, nevertheless, is not unreasonable for a fossil system expected to form earlier than the general cluster population. Hence, RXJ 1159+5531 appears to be an optimal, benchmark cluster for hydrostatic studies of its ICM.

We thank the anonymous referee for several helpful comments and suggestions, including the suggestion that we make the comparison shown in the right panel of Figure 7. D.A.B. and Y. S. gratefully acknowledge partial support from the National Aeronautics and Space Administration under grants NNX13AF14G and NNX15AM97G issued through the Astrophysics Data Analysis Program. Partial support for this work was also provided by NASA through Chandra Award Nos. GO2-13159X and GO4-15117X issued by the Chandra X-ray Observatory Center, which is operated by the Smithsonian Astrophysical Observatory for and on behalf of NASA under contract NAS8-03060. The scientific results reported in this article are based in part on observations made by the *Chandra X-ray Observatory* and by the *Suzaku* satellite, a collaborative mission between the space agencies of Japan (JAXA) and the USA (NASA). This research has made use of the NASA/IPAC Extragalactic Database (NED) which is operated by the Jet Propulsion Laboratory, California Institute of Technology, under contract with the National Aeronautics and Space Administration.

REFERENCES

Allen, S. W., Evrard, A. E., & Mantz, A. B. 2011, ARA&A, 49, 409
Anders, E., & Grevesse, N. 1989, GeCoA, 53, 197
Angus, G. W., Famaey, B., & Buote, D. A. 2008, MNRAS, 387, 1470
Arnaud, K. A. 1996, in ASP Conf. Ser. 101, Astronomical Data Analysis Software and Systems V, ed. G. H. Jacoby & J. Barnes (San Francisco, CA: ASP), 17
Arnaud, M., Pratt, G. W., Piffaretti, R., et al. 2010, A&A, 517, A92
Asplund, M., Grevesse, N., & Jacques Sauval, A. 2006, NuPhA, 777, 1
Auger, M. W., Treu, T., Bolton, A. S., et al. 2010, ApJ, 724, 511
Bell, E. F., McIntosh, D. H., Katz, N., & Weinberg, M. D. 2003, ApJS, 149, 289
Blumenthal, G. R., Faber, S. M., Flores, R., & Primack, J. R. 1986, ApJ, 301, 27
Buote, D. A. 2000a, ApJ, 539, 172
Buote, D. A. 2000b, MNRAS, 311, 176
Buote, D. A., Gastaldello, F., Humphrey, P. J., et al. 2007, ApJ, 664, 123
Buote, D. A., & Humphrey, P. J. 2012a, in Astrophysics and Space Science Library, Vol. 378, Hot Interstellar Matter in Elliptical Galaxies, ed. D.-W. Kim & S. Pellegrini (New York: Springer), 235
Buote, D. A., & Humphrey, P. J. 2012b, MNRAS, 421, 1399
Bykov, A. M., Churazov, E. M., Ferrari, C., et al. 2015, SSRv, 188, 141
Cappellari, M., Romanowsky, A. J., Brodie, J. P., et al. 2015, ApJL, 804, L21
Chabrier, G. 2003, ApJL, 586, L133
Conroy, C., & van Dokkum, P. G. 2012, ApJ, 760, 71
Courteau, S., Cappellari, M., de Jong, R. S., et al. 2014, RvMP, 86, 47
De Luca, A., & Molendi, S. 2004, A&A, 419, 837
Démoclès, J., Pratt, G. W., Pierini, D., et al. 2010, A&A, 517, A52
Dickey, J. M., & Lockman, F. J. 1990, ARA&A, 28, 215
Dutton, A. A., & Macciò, A. V. 2014, MNRAS, 441, 3359
Dutton, A. A., & Treu, T. 2014, MNRAS, 438, 3594
Eckert, D., Ettori, S., Coupon, J., et al. 2015, arXiv:1512.03814
Einasto, J. 1965, TrAlm, 5, 87
Ettori, S. 2015, MNRAS, 446, 2629
Ettori, S., Donnarumma, A., Pointecouteau, E., et al. 2013, SSRv, 177, 119
Feroz, F., Hobson, M. P., & Bridges, M. 2009, MNRAS, 398, 1601
Gastaldello, F., Buote, D. A., Humphrey, P. J., et al. 2007, ApJ, 669, 158
Girardi, M., Aguerri, J. A. L., De Grandi, S., et al. 2014, A&A, 565, A115
Gnedin, O. Y., Kravtsov, A. V., Klypin, A. A., & Nagai, D. 2004, ApJ, 616, 16
Humphrey, P. J., & Buote, D. A. 2010, MNRAS, 403, 2143
Humphrey, P. J., Buote, D. A., Brighenti, F., Gebhardt, K., & Mathews, W. G. 2008, ApJ, 683, 161
Humphrey, P. J., Buote, D. A., Brighenti, F., Gebhardt, K., & Mathews, W. G. 2009, ApJ, 703, 1257
Humphrey, P. J., Buote, D. A., Brighenti, F., et al. 2012a, ApJ, 748, 11
Humphrey, P. J., Buote, D. A., Canizares, C. R., Fabian, A. C., & Miller, J. M. 2011, ApJ, 729, 53
Humphrey, P. J., Buote, D. A., Gastaldello, F., et al. 2006, ApJ, 646, 899
Humphrey, P. J., Buote, D. A., O'Sullivan, E., & Ponman, T. J. 2012b, ApJ, 755, 166
Jarrett, T. H., Chester, T., Cutri, R., et al. 2000, AJ, 119, 2498
Khosroshahi, H. G., Maughan, B. J., Ponman, T. J., & Jones, L. R. 2006, MNRAS, 369, 1211
Kitayama, T., Bautz, M., Markevitch, M., et al. 2014, arXiv:1412.1176
Kravtsov, A. V., & Borgani, S. 2012, ARA&A, 50, 353
Laporte, C. F. P., & White, S. D. M. 2015, MNRAS, 451, 1177
Le Brun, A. M. C., McCarthy, I. G., Schaye, J., & Ponman, T. J. 2014, MNRAS, 441, 1270
Lodders, K. 2003, ApJ, 591, 1220
Loeb, A., & Peebles, P. J. E. 2003, ApJ, 589, 29
Mamon, G. A., & Łokas, E. L. 2005, MNRAS, 362, 95
Mazzotta, P., Rasia, E., Moscardini, L., & Tormen, G. 2004, MNRAS, 354, 10
McLaughlin, D. E. 1999, AJ, 117, 2398
Merritt, D., Graham, A. W., Moore, B., Diemand, J., & Terzić, B. 2006, AJ, 132, 2685
Milgrom, M. 1983, ApJ, 270, 365
Milgrom, M. 2015, MNRAS, 454, 3810
Nagai, D., Vikhlinin, A., & Kravtsov, A. V. 2007, ApJ, 655, 98
Navarro, J. F., Frenk, C. S., & White, S. D. M. 1997, ApJ, 490, 493
Newman, A. B., Ellis, R. S., & Treu, T. 2015, arXiv:1503.05282
Newman, A. B., Treu, T., Ellis, R. S., & Sand, D. J. 2013a, ApJ, 765, 25
Newman, A. B., Treu, T., Ellis, R. S., et al. 2013b, ApJ, 765, 24
Nulsen, P. E. J., & Bohringer, H. 1995, MNRAS, 274, 1093
Parrish, I. J., McCourt, M., Quataert, E., & Sharma, P. 2012, MNRAS, 419, L29
Planck Collaboration, Ade, P. A. R., Aghanim, N., et al. 2014, A&A, 571, A16
Pointecouteau, E., Arnaud, M., & Pratt, G. W. 2005, A&A, 435, 1
Pointecouteau, E., & Silk, J. 2005, MNRAS, 364, 654
Pratt, G. W., Arnaud, M., Piffaretti, R., et al. 2010, A&A, 511, A85
Purcell, C. W., Bullock, J. S., & Zentner, A. R. 2007, ApJ, 666, 20

Rasia, E., Borgani, S., Ettori, S., Mazzotta, P., & Meneghetti, M. 2013, ApJ, 776, 39
Rasia, E., Tormen, G., & Moscardini, L. 2004, MNRAS, 351, 237
Reiprich, T. H., Basu, K., Ettori, S., et al. 2013, SSRv, 177, 195
Retana-Montenegro, E., van Hese, E., Gentile, G., Baes, M., & Frutos-Alfaro, F. 2012, A&A, 540, A70
Sanders, R. H. 1999, ApJL, 512, L23
Sarazin, C. L. 1986, RvMP, 58, 1
Schneider, M. D., Frenk, C. S., & Cole, S. 2012, JCAP, 5, 030
Smith, R. J., Lucey, J. R., & Conroy, C. 2015, MNRAS, 449, 3441
Su, Y., Buote, D., Gastaldello, F., & Brighenti, F. 2015, ApJ, 805, 104
Su, Y., Gu, L., White, R. E., III, & Irwin, J. 2014, ApJ, 786, 152
Tozzi, P., & Norman, C. 2001, ApJ, 546, 63
Umetsu, K., Zitrin, A., Gruen, D., et al. 2015, arXiv:1507.04385
Vikhlinin, A., Kravtsov, A., Forman, W., et al. 2006, ApJ, 640, 691
Vikhlinin, A., McNamara, B. R., Hornstrup, A., et al. 1999, ApJL, 520, L1
Voit, G. M., Kay, S. T., & Bryan, G. L. 2005, MNRAS, 364, 909
Zappacosta, L., Buote, D. A., Gastaldello, F., et al. 2006, ApJ, 650, 777
Zhang, Z., Xu, H., Wang, Y., et al. 2007, ApJ, 656, 805
Zibetti, S., Charlot, S., & Rix, H.-W. 2009, MNRAS, 400, 1181